

Model Reduction of a Piecewise Linear Flexible Mechanical Oscillator

Suparno Bhattacharyya and Joseph. P. Cusumano*

Department of Engineering Science and Mechanics
Pennsylvania State University

November 28, 2023
Submitted for review

Abstract

We study the reduced order modeling of a nonlinear flexible oscillator in which a Bernoulli-Euler beam with a permanent tip magnet is subjected to a position-triggered electromagnetic kick force. This results in non-smooth boundary conditions capable of exciting many degrees of freedom. The system is modeled as piecewise linear with the different boundary conditions determining different regions of a hybrid phase space. With kick strength as parameter, its bifurcation diagram is found to exhibit a range of periodic and chaotic behaviors. Proper orthogonal decomposition (POD) is used to estimate the system's intrinsic dimensionality. However, conventional POD's purely statistical analysis of spatial covariance does not guarantee accuracy of reduced order models (ROMs). We therefore augment POD by employing a previously-developed energy closure criterion that selects ROM dimension by ensuring approximate energy balance on the reduced subspace. This physics-based criterion yields accurate ROMs with 8 degrees of freedom. Remarkably, we show that ROMs formulated at particular values of the kick strength can nevertheless reconstruct the entire bifurcation structure of the original system. Our results demonstrate that energy closure analysis outperforms variance-based estimates of effective dimension for nonlinear structural systems, and is capable of providing ROMs that are robust even across stability transitions.

1 Introduction

Reduced order models (ROMs) play a crucial role in capturing the dominant dynamics of high-dimensional systems, thereby facilitating efficient computational analyses such as uncertainty propagation, optimization, and control. However, accurately estimating the dimension of these models, a key determinant of their accuracy, remains a challenge. Conventionally, the dimension of a ROM formulated using proper orthogonal decomposition

*Address correspondence to: jpc3@psu.edu.

(POD) is determined by selecting a subspace that captures a substantial percentage of the total data variance [1, 2]. In previous work [3, 4], we identified the limitations of such variance-based dimension estimation when applied to structural systems subjected to impulsive loading. As an enhancement to conventional POD, we proposed a physics-based criterion, where the model subspace is chosen to ensure a balance between the energy input and dissipated from the associated reduced subspace.

In this study, we apply this *energy closure* approach to dimension reduction of a more complex system: a magnetically kicked flexible oscillator, as depicted in Fig. 1, that at the first principles level is both infinite dimensional and hybrid. The physical system consists of a thin steel beam with a permanent magnet at its tip, to which an electromagnet applies a position-triggered kick force during oscillations. This magnetic interaction is only significant when the beam tip is in the vicinity of the electromagnet, and rapidly decays as the tip moves away. Thus, the boundary conditions are piecewise and, therefore, nonsmooth. We model the dynamics of this system as a piecewise linear, but globally nonlinear, flexible oscillator. Thus, this system serves as an example for engineering applications where system components intermittently interact with constraints and/or actuators, such as might occur with backlashes or clearances, active or passive car suspension systems, nonlinear vibration absorbers, gear boxes, bearings, etc. The objective of this study is twofold: firstly, we aim to examine the dynamics of this autonomous hybrid flexible system, particularly regarding its bifurcation structure; and, secondly, we seek to study the efficacy of the energy closure criterion in providing ROMs that accurately capture its behavior.

There has been significant interest in investigating the dynamics of piecewise oscillators subject to periodic external forcing and/or impacts, both theoretically and experimentally [5–25]; however the model reduction of such systems remains a little-studied problem. Prior experimental studies of the kicked, autonomous oscillator that is the focus of this paper [26, 27] demonstrated that the physical system exhibits periodic, quasiperiodic, and chaotic steady states, depending on the magnetic kick strength; additionally, POD applied to time-series data gathered from different locations on the beam was used to study low-dimensional modal interactions of the system.

In addition to exhibiting a range of steady state behaviors, the dynamics of piecewise flexible oscillators are, in general, expected to be high-dimensional, especially when lightly damped. This is because numerous degrees of freedom (DOFs) can be excited during transitions or “events” demarcating regions of the system’s hybrid state space. Furthermore, the system’s effective dimension cannot be known beforehand. Thus, computationally studying the dynamics of such systems can be expensive since numerical solution methods, such as the finite element method, typically will involve a large number of degrees of freedom. Hence, for such systems, reduced order modeling remains essential for efficient analysis.

There has been a recent surge in data-driven model reduction methods, particularly those leveraging neural networks, such as deep learning-based reduced order models [28–36]. While these emerging methodologies promise to broaden the horizons for handling complex systems, their general application is still an area of active research, especially in the context of nonlinear structural vibrations. For model reduction in this work, we applied

the well-established proper orthogonal decomposition (POD) [1, 2, 37–45], also referred to as the Karhunen-Loève decomposition [46–52], in which spatial correlation analysis is used to obtain a least-squares optimal projection of governing equations onto a linear subspace spanned by proper orthogonal modes (POMs). This approach has a solid theoretical foundation and provides a useful blend of computational efficiency and physical interpretability. To this foundational method, we add the energy closure criterion [3, 4], which provides a strong linkage to the system’s underlying physics, something that is absent from purely statistical data-driven approaches.

The remainder of the paper is structured as follows: we first model the kicked-oscillator, followed by a discussion of its steady-state dynamics and bifurcation structure. We then carry out the model reduction procedure using POD with energy closure dimension estimation. We conclude by simulating the reduced order model and comparing its behavior to the original system.

2 Model formulation and piecewise solution

Figure 1a depicts the experimental oscillator comprising a thin steel beam with dimensions 6.5 in \times 0.5 in \times 0.009 in (16.5 cm \times 1.27 cm \times 0.023 cm) [26]. The beam is clamped at the top and its neutral axis is aligned vertically in the rest configuration. A 0.127 in thick \times 0.5 in diameter (0.32 cm \times 1.27 cm) rare-earth permanent magnet is firmly attached at the free end of the beam, which modifies the beam’s free boundary conditions through a combination of inertial and generalized restoring forces near the tip. The rare-earth magnet interacts with a “kicker” electromagnet, the steel core of which is 0.225 in (0.57 cm) in diameter, located approximately 0.06 in (0.15 cm) from the permanent magnet.

When the beam tip moves over the electromagnet at a velocity greater than a certain critical velocity, v_{cr} , a sensor coil activates a Hall-effect transistor that supplies power to the electromagnet. This in turn applies a generalized force to the tip of the beam as it moves over the core. The magnitude of this force, which is the kick strength, is controlled experimentally by the DC voltage applied to the kicker magnet coil. Given that the kicker electromagnet is spatially triggered, the system is autonomous. In addition to the kick, there is a strong and strongly nonlinear restoring force at the tip of the beam when the permanent magnet at its tip is near the ferromagnetic core of the electromagnet. However, both the kick and the restoring forces rapidly diminish to zero when the tip’s position exceeds the radius of the core.

We model this experimental system as being piecewise linear (Fig. 1b). The dynamics of the beam is modeled using the dimensionless Bernoulli-Euler beam equation (see Appendix A for rescaling):

$$w''''(x, t) + \ddot{w}(x, t) + c_m \dot{w}''''(x, t) + c_v \dot{w}(x, t) = 0, \quad (1)$$

where: $w(x, t)$ ($x \in [0, 1]$) denotes the dimensionless horizontal deflection of the beam during oscillations as measured from the vertical neutral axis; the primes and overdots indicate dimensionless spatial and temporal derivatives, respectively; and c_m and c_v denote

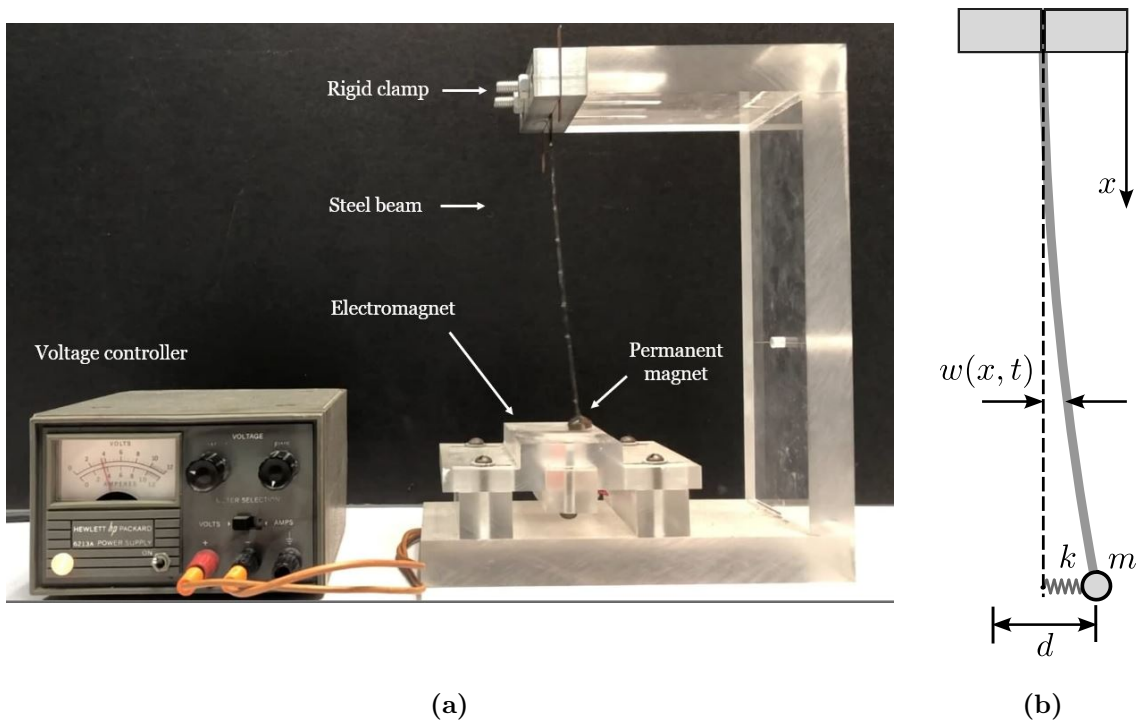


Figure 1: Kicked beam flexible oscillator: (a) experimental setup (see text for detailed description); (b) the piecewise Bernoulli-Euler beam model with displacement $w(x, t)$. The permanent magnet at the beam tip is modeled as a point mass m ; the spring to ground has stiffness k ; and dimension d indicates the size of the kicking region (the diameter of the kicker magnet core). Not indicated is the piecewise nature of the restoring and applied forces at that tip, which yield hybrid boundary conditions (Eqs. 2) and phase space (see Fig. 2).

the dimensionless coefficients of material and viscous damping, respectively.

As described above, the boundary conditions for Eq. (1) depend on the configuration of the beam. The situation can be precisely summarized using the position-velocity phase plane at the beam’s tip (i.e., at $x = 1$), as illustrated in Fig. 2, which shows eight distinct regions with different boundary conditions, each of which are modeled as follows.

In regions 2 and 6, the force between the tip magnet, modeled as a point mass m , and kicker magnet core is negligible. As a result, the beam at $x = 1$ is only subjected to the inertial force arising from the acceleration of the permanent magnet. In regions 3 and 7, there is no kick force because the tip velocity fails to trigger the electromagnet (that is, $|\dot{w}(1, t)| < v_{cr}$); however, the restoring force between the iron core and tip magnet is active. We model this force by a linear spring from the tip to ground (Fig. 1b). As a result, the boundary condition at $x = 1$ includes both the inertial and generalized restoring forces. The same is true for regions 1 and 5. In regions 4 and 8, the tip velocity magnitude $|\dot{w}(1, t)| > v_{cr}$, so the system is subjected to a force boundary condition from the electromagnet. We model this magnetic “kick” as a constant generalized force at the beam tip. We further impose the condition

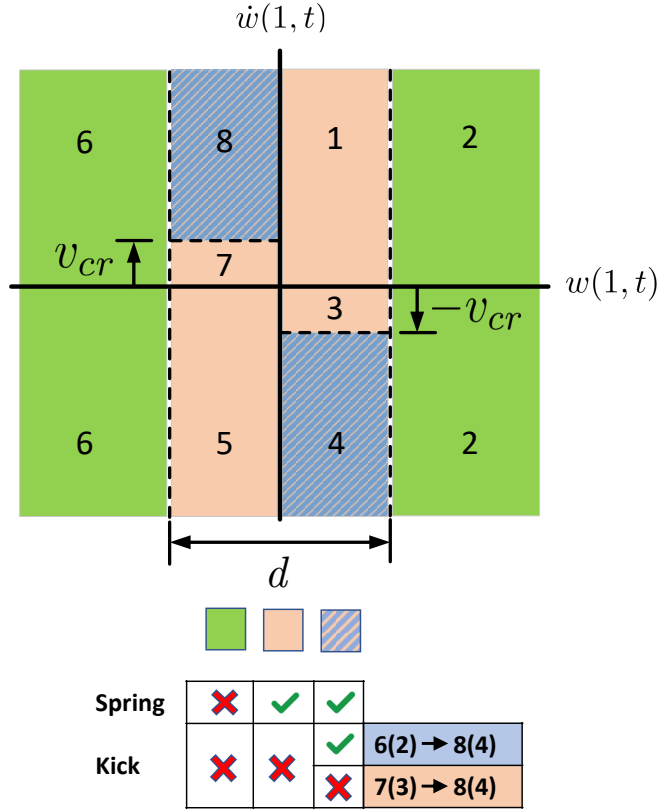


Figure 2: Regions in the displacement-velocity phase plane for beam tip corresponding to different boundary conditions: in regions 2 and 6, the tip is only subjected to the inertial force owing to the acceleration of the permanent magnet; in regions 3 and 7 it is subjected to a combination of the inertial and a generalized magnetic restoring force is modeled as a linear spring (see Fig. 1); in regions 4 and 8, in addition to the inertial and restoring forces, the tip is acted upon by the kick force coming from the electromagnet. If an orbit on the phase plane enters region 8 (or 4) from region 7 (or 3) instead of region 6 (or 2), then the kick force is not activated and region 8 (or 4) becomes an extension of region 7 (or 3). Thus, three separate models are used to describe the dynamics of the oscillator: model A describes the behavior in regions 2 and 6, model B in regions 4 and 8, and model C in the remaining regions.

that if the beam's tip trajectory enters region 8 (or 4) from region 7 (or 3), instead of via region 6 (or 2), the kick force is not activated, so that region 8 (or 4) has the same boundary condition as in region 7 (or 3).

The above boundary conditions can then be summarized as follows (refer to Fig. 2):

$$w(0, t) = 0 \quad (2a)$$

$$w'(0, t) = 0 \quad (2b)$$

$$w''(1, t) + c_m \dot{w}''(1, t) = 0 \quad (2c)$$

$$w'''(1, t) + c_m \dot{w}'''(1, t) = \begin{cases} m\ddot{w}(1, t) & \text{in regions 2, 6} \\ kw(1, t) + m\ddot{w}(1, t) + \text{sgn}(\dot{w}(1, t))F & \text{in regions 4, 8} \\ kw(1, t) + m\ddot{w}(1, t) & \text{in regions 1, 3, 5, 7} \end{cases} \quad (2d)$$

in which: m denotes the dimensionless mass of the permanent magnet; k denotes the dimensionless stiffness of the spring modeling the magnetic restoring force at the beam tip, and F is the dimensionless kick force generated from the electromagnet (see Appendix A). Note that in regions 4 and 8 (Eq. 2d) the kick force F acts in same direction as the tip velocity.

These boundary conditions result in three linear models that we label as A, B, and C. Together, these models describe the nonlinear dynamics of the oscillator in its hybrid phase space. Model A describes the behavior of the system in regions 2 and 6, when the tip is far from the kicker magnet, so there is no tip force (refer to Fig. 2 and the cases of Eq. 2d). The other two models incorporate the effect of the magnetic interaction: model B describes the behavior in regions 4 and 8, in which both the kick force and magnetic restoring force are active; model C describes the dynamics of the beam in regions 1, 3, 5, 7, in which only the magnetic restoring force is active.

2.1 Weak formulation of the governing equations

Equation (1), along with the boundary conditions of Eq. (2), represents the strong form of the piecewise initial boundary value problem (IBVP) in the displacement w . We aim to determine the solution of the IBVP using the Ritz method [53] by first deriving the system's weak form [54]. Let $q(x)$ be selected from a space of trial functions satisfying the essential boundary conditions and having square-integrable spatial derivatives up to second order. We then express the weak form of the IBVP as:

$$([\ddot{w} + w'''' + c_v \dot{w} + c_m \dot{w}''''], q) = 0 \quad (3)$$

where (\cdot, \cdot) denotes the standard inner product in L^2 . Integrating by parts and employing the boundary conditions we obtain

$$\int_0^1 \ddot{w}(x, t)q(x) dx + c_v \int_0^1 \dot{w}(x, t)q(x) dx + c_m \int_0^1 \dot{w}''(x, t)q''(x) dx + \int_0^1 w''(x, t)q''(x) dx + \mathcal{I} = 0 \quad (4)$$

Where \mathcal{I} is defined as (refer to Fig. 2 and Eq. (2d)):

$$\mathcal{I} = \begin{cases} m\ddot{w}(1, t)q(1) & \text{for Model A} & (5a) \\ (kw(1, t) + m\ddot{w}(1, t) + \text{sgn}(\dot{w}(1, t))F)q(1) & \text{for Model B} & (5b) \\ (kw(1, t) + m\ddot{w}(1, t))q(1) & \text{for Model C.} & (5c) \end{cases}$$

To derive an approximate numerical solution to these weak IBVPs, one chooses a suitable basis for the space of trial functions, and writes $w(x, t)$ as an expansion in terms of N of the basis functions. Substituting this expansion into Eq. (4) transforms our weak IBVP into a piecewise initial value problem (IVP) with a system of N second-order ODEs valid in each region of the phase space. The solutions to this piecewise system provide the coordinates of each basis function needed to determine and approximation to $w(x, t)$. In principle, this can be done using either a localized basis, as with finite element analysis, or a global basis, as with modal analysis. Owing to the relatively simple structure of our system, we elected to use the latter, as described in the next section.

2.2 Piecewise solution to the weak boundary value problem

To obtain the linear normal modes for each model, we first estimate the associated natural frequencies. In all cases, the characteristic equation can be written in the general form:

$$(\mathcal{A} - \mathcal{B}) \exp(-2\beta) + (\mathcal{A} + \mathcal{B}) + 2\beta^3 \exp(-\beta) = 0, \quad (6)$$

where

$$\mathcal{A} = \beta^3 \cos(\beta) + k \sin(\beta) + \beta^4 (-m) \sin(\beta), \quad (7a)$$

$$\mathcal{B} = \beta^4 m \cos(\beta) - k \cos(\beta), \quad (7b)$$

and $\beta_i = \sqrt{\omega_i}$, where ω_i denotes the i^{th} natural frequency of the beam.

For models B and C, the characteristic equation Eq. (6) is the same because the constant force F at the boundary corresponding to model B can be eliminated by first calculating the solution of its PDE about the static deflection curve resulting from F (see Appendix B). The natural frequencies in these cases are denoted as by ω_i . For model A, Eqs. (6) and (7) are modified by setting $k = 0$ and the natural frequencies are denoted by Ω_i .

Equation (6) was used to numerically solve for the natural frequencies, which were then used to obtain the normal modes [55, 56]. Denoting the i^{th} mode for model A as γ_i , and for models B and C as ξ_i , N -mode approximations for $w(x, t)$ have the form:

$$w(x, t) = \begin{cases} \sum_{i=1}^N r_i(t) \gamma_i(x) & \text{for model A} & (8a) \\ \sum_{i=1}^N a_i(t) \xi_i(x) & \text{for model B} & (8b) \\ \sum_{i=1}^N \alpha_i(t) \xi_i(x) & \text{for model C.} & (8c) \end{cases}$$

Starting with the eigenvalue problem in each case, standard manipulations (the general form of which can be found in Appendix C) lead to the following orthonormality conditions:

$$\int_0^1 \gamma_i \gamma_j dx + m \gamma_i(1) \gamma_j(1) = \delta_{ij}, \quad (9a)$$

$$\int_0^1 \gamma_j'' \gamma_i'' dx = \Omega_i^2 \delta_{ij}, \quad (9b)$$

$$\int_0^1 \xi_i \xi_j dx + m \xi_i(1) \xi_j(1) = \delta_{ij}, \quad (9c)$$

$$\int_0^1 \xi_i'' \xi_j'' dx + k \xi_i(1) \xi_j(1) = \omega_i^2 \delta_{ij}. \quad (9d)$$

Using the computed normal modes in the expansions of Eqs. (8), substituting into Eq. (4), and integrating yields coupled ordinary differential equations (ODEs) for each model. For example, with model C, Eq. (8c) yields

$$\sum_{i=1}^N \left\{ \ddot{\alpha}_i \int_0^1 \xi_i \xi_j dx + \alpha_i \int_0^1 \xi_i'' \xi_j'' dx + c_v \dot{\alpha}_i \int_0^1 \xi_i \xi_j dx + c_m \dot{\alpha}_i \int_0^1 \xi_i'' \xi_j'' dx \right. \\ \left. + (k \alpha_i \xi_i(1) + m \ddot{\alpha}_i \xi_i(1)) \xi_j(1) \right\} = 0 \quad (10)$$

Then, Eqs. (9c) and (9d) yield N ODEs as:

$$\sum_{i=1}^N \left\{ \delta_{ij} (\ddot{\alpha}_i + \omega_i^2 \alpha_i) + c_v \dot{\alpha}_i \int_0^1 \xi_i \xi_j dx + c_m \dot{\alpha}_i \int_0^1 \xi_i'' \xi_j'' dx \right\} = 0 \\ \implies \ddot{\alpha}_j + (c_v + c_m \omega_j^2) \dot{\alpha}_j + \sum_{i=1}^N D_{ij} \alpha_i + \omega_j^2 \alpha_j = 0 \quad (j = 1, 2, \dots, N), \quad (11)$$

in which the matrix with elements $D_{ij} = -\xi_i(1) \xi_j(1) (m c_v + k c_m)$ represents non-proportional damping arising from the $x = 1$ boundary condition. Hence, the system is not diagonalizable: that is, all of its normal modes are coupled through the damping. The ODEs for Model B have the same form as Eq. (11) for displacements relative to the static deflection curve for constant F , as described above. Similarly, using Eqs. (9a) and (9b) one obtains the ODEs for model A, which have the same form as Eq. (11), but with $k = 0$, normal modes ξ_i replaced by γ_i , and natural frequencies ω_i replaced by Ω_i .

At the beginning of a simulation, a specific model is chosen depending on where the initial position and velocity of the tip of the beam is located. This is used to obtain the dynamics of the beam until its tip hits a transition boundary, either at $w(1, t) = 0$ or $|w(1, t)| = d/2$ (Figs. 1 and 2). The state at the transition is transferred to the new region's model and subsequent dynamics is computed.

For example, consider that the initial configuration of the beam is such that the tip of the beam is in region 2 (Fig. 2). In this case, model A is used to describe the dynamics of the beam. As the system state evolves in time, the trajectory eventually enters region 3 or 4

in the phase plane, depending on the velocity of the tip. The time t_R at which the tip of the beam reaches the transition boundary is estimated from $|w(1, t_R)| = d/2$ using model A and the bisection root finding algorithm. Across the boundary, the full state of model A must be passed to the next model. Hence, assuming, for example, that the beam tip enters region 3, at the transition from model A to model B at $t = t_R$, the following must hold:

$$\begin{aligned} w(x, t_R) &= \sum_{i=1}^N r_i(t_R) \gamma_i(x) = \sum_{j=1}^N a_j(0) \xi_j(x) \\ \dot{w}(x, t_R) &= \sum_{i=1}^N \dot{r}_i(t_R) \gamma_i(x) = \sum_{j=1}^N \dot{a}_j(0) \xi_j(x). \end{aligned} \tag{12}$$

Note that we can take $t = 0$ in the post-transition model because the system is autonomous. This implies that

$$\begin{aligned} a_i(0) &= \sum_{j=1}^N G_{ij} r_j(t_R) \\ \dot{a}_i(0) &= \sum_{j=1}^N G_{ij} \dot{r}_j(t_R) \end{aligned} \tag{13}$$

where $G_{ij} = \int_0^1 \gamma_i(x) \xi_j(x) dx + m \gamma_i(1) \xi_j(1)$. These initial conditions for the new modal coordinates are then used to calculate the subsequent dynamics using model B. This same approach is adopted for dealing with other similar transitions for the duration of the simulation.

3 Dynamics of the kicked oscillator

For this study, the “exact” solutions to the hybrid system of Eqs. (4) and (5) were obtained using the finite-dimensional expansions of Eqs. (8) with $N = 25$ normal modes in all three models. MATLAB’s native solver, `ode45`, was used to integrate the resulting ordinary differential equations. No attempt was made to exactly match our model parameters to the physical experiment (Fig. 1a), rather our interest was in exploring the model’s general, qualitative behavior. After initial experimentation with the numerical model, we selected $m = 1$, $d = 0.2$, and $v_{cr} = 0.05$. We also set $k = 1000$ (the ratio of the stiffness to ground at the tip vs. the internal stiffness of the beam), $c_v = 4.5$ (the coefficient of viscous damping), and $c_m = 3 \times 10^{-4}$ (the coefficient of material damping) for simulations. Keeping these parameters fixed for all simulations, we varied the kick strength F and recorded various responses of the system. We collected discrete samples in space and time of the simulated response, $w(x, t)$, at $N_\Omega = 100$ uniformly spaced points along the beam, with a sampling frequency $f_s = 1000$ samples/unit time.

Different attracting steady-state solutions of the system are summarized by the bifurcation diagram of Fig. 3, in which the kick strength F is the bifurcation parameter. The bifurcation

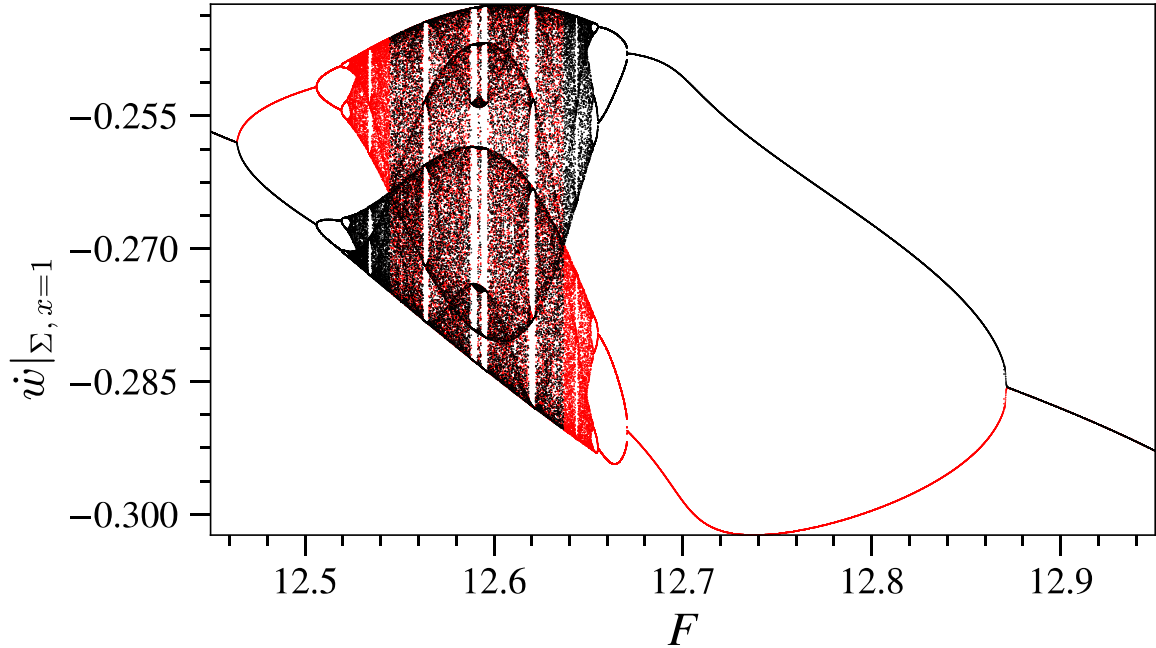


Figure 3: Bifurcation diagram of the kicked oscillator obtained from simulating the piecewise-linear system of Eqs. (4) and (5) for kick strength $F \in [12.45, 12.95]$. “Exact” solutions were computed using Ritz approximations with $N = 25$ linear normal modes (Section 2.2). The diagram was constructed on the Poincaré section Σ (Eq. 14) using branch-following continuation. The other parameter values used in the simulations were: $c_v = 4.5$, $c_m = 3 \times 10^{-4}$, $m = 1$, $k = 1000$, $d = 0.2$, $v_{cr} = 0.05$. Two solution branches are shown in the figure: the red branch was obtained by starting at $F = 12.95$ and *decreasing* the kick force, whereas the black branch was obtained by starting at $F = 12.45$ and *increasing* its value.

diagram is constructed on a fixed Poincaré section [57] in the state space, defined by

$$\Sigma = \{ (w(x, t), \dot{w}(x, t)) \mid w(1, t) = d/2; \dot{w}(1, t) < 0 \}. \quad (14)$$

For each value of F , the tip velocity, $\dot{w}(1, t)$ of the steady state at each intersection with Σ is plotted. Period- n solutions have n distinct points for the associated value of F , whereas chaotic solutions have a theoretically infinite number of points: for Fig. 3, we plotted a maximum of 16 distinct points for each F .

Starting with $F = 12.95$, the entire bifurcation diagram was constructed using simple branch-following continuation [58] with $\Delta F = 5 \times 10^{-5}$, resulting in a total of 10^4 values of F on the bifurcation diagram. The solution branch thus obtained is shown in red in Fig. 3. The other solution branch shown using black was obtained by starting the same algorithm from $F = 12.45$ and increasing F until $F = 12.95$ with the same ΔF .

In Fig. 3, we observe that for $F \gtrsim 12.88$, all trajectories converge to the same period-1 limit cycle: both solution branches are merged in this regime. In Fig. 4a, the limit cycle corresponding to $F \approx 12.95$ is plotted on the phase plane at the beam’s tip. We observe

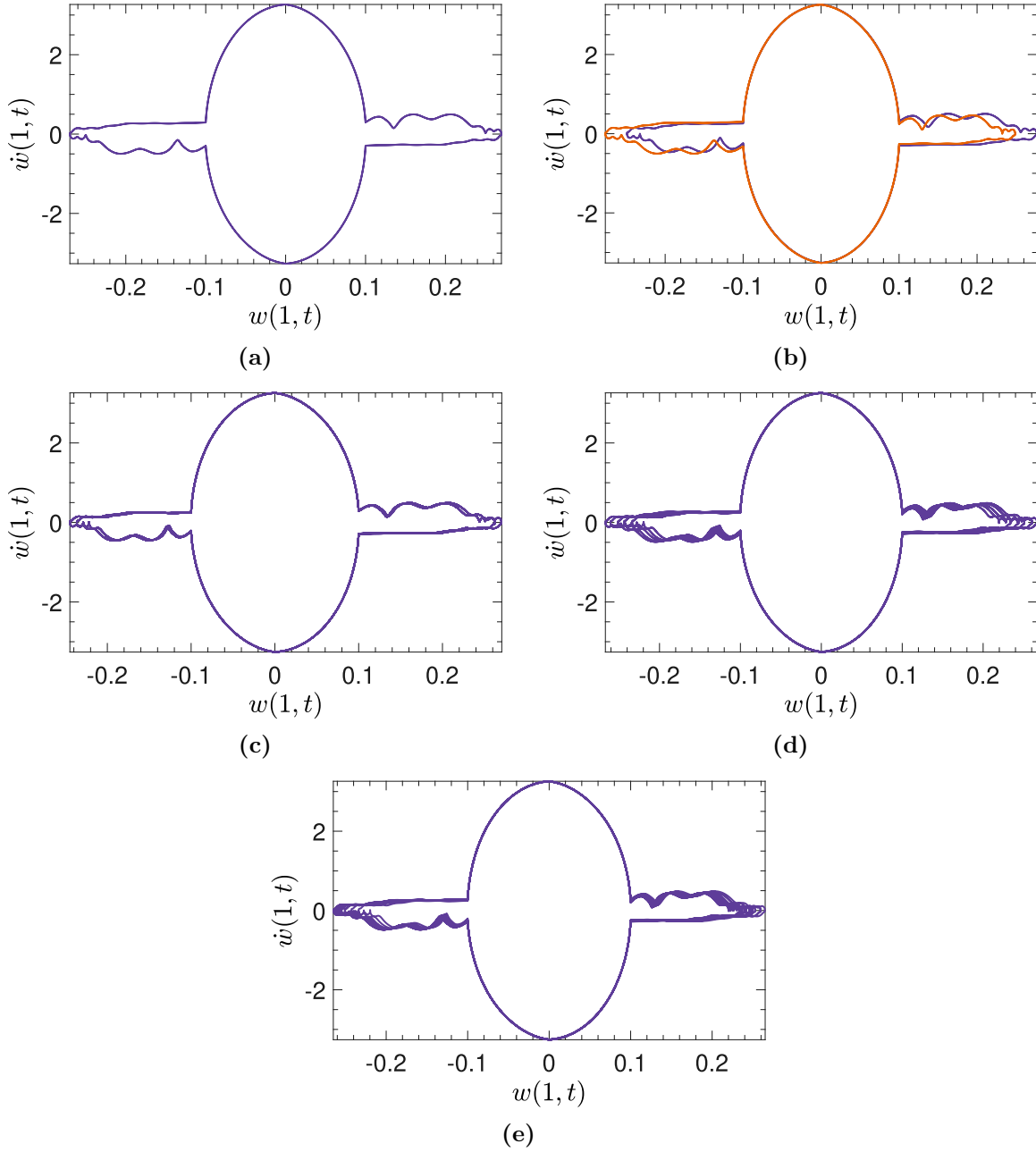


Figure 4: Different steady state solutions plotted on the phase plane of the beam tip for different kick strengths F (see bifurcation diagram Fig. 3): (a) period-1 limit cycle for $F \approx 12.95$; (b) two period-1 limit cycles from different solution branches (indicated by red and black in Fig. 3) for $F \approx 12.75$; (c) period-2 orbit for $F \approx 12.66$; (d) period-5 orbit for $F \approx 12.621$; (e) chaotic orbit for $F \approx 12.605$. All orbits, except for those in (b), are symmetric when reflected across both the $w(1,t)$ and $\dot{w}(1,t)$ axes, consistent with the invariance system (Eqs. 1 and 2) under $w \rightarrow -w$ and $\dot{w} \rightarrow -\dot{w}$. The two asymmetric limit cycles in (b), taken together, recover full symmetry of the system. Except for F , the remaining parameters used to construct these plots are the same as used for Fig. 3.

that the limit cycle is symmetric under reflections across both the $w(1, t)$ and $\dot{w}(1, t)$ axis. This is not surprising, since the governing equations possess this symmetry, which is evident from the invariance of the PDE (Eq. 1) and boundary conditions (Eq. 2) under the transformation $w \rightarrow -w$ and $\dot{w} \rightarrow -\dot{w}$. The shape of the orbit is oval-shaped when $|w(1, t)| \leq d/2 = 0.1$, in the region over the kicker-magnet, and the trajectory has little or no “wiggles” related to higher-frequency components of the oscillations, consistent with only a few modes being excited in this region. Immediately outside this region, however, where the magnetic attraction and the kick force sharply drop to zero, more “wiggles” are observed in the “wing” shaped segments of the orbit, as the tip crosses from region 4 (or 8) to 5 (or 1). This suggests that the nonsmooth transition has excited a larger number of modes. Nondifferentiable “kinks” in the orbits occur in two ways: the more obvious case occurs when all magnetic interactions at the tip suddenly drop to zero whenever $|w(1, t)|$ exceeds $d/2 = 0.1$; the more subtle case occurs when the kick force suddenly turns off as $w(1, t)$ crosses zero in either direction.

As the value of F is decreased, the amplitude of the period-1 limit cycle decreases until $F \approx 12.88$, at which we observe two period-1 solution branches emerge and continue until $F \approx 12.68$. This does *not* indicate doubling but, rather, a symmetry-breaking bifurcation in which two, distinct asymmetric period-1 orbits are created. In Fig. 4b, we plot both of these orbits from both branches, corresponding to $F \approx 12.75$: unlike in Fig. 4a, these individual solutions do not possess reflectional symmetry across the plane’s axes; however, taken together, they recover the full system symmetry.

Below $F \approx 12.68$, we observe period-doubling bifurcation sequences in both branches. In Fig. 4c, we show a period-2 orbit appearing after the first period doubling in the lower (red) branch at $F \approx 12.66$. As F is further decreased, the period doubling both branches leads to chaotic regimes. Eventually, for $12.545 \lesssim F \lesssim 12.635$, both solution branches merge and lead to a single chaotic regime with full symmetry, with brief windows containing multi-period solutions. In Figs. 4d and 4e, we show a period-5 and a chaotic orbit on the phase plane plot of the beam tip, corresponding to $F \approx 12.621$ and $F \approx 12.605$, respectively. For $F \lesssim 12.545$, we again observe two different solution branches undergoing period halving bifurcation separately and merging into a single branch for $F \lesssim 12.52$. This branch does not continue beyond $F \lesssim 12.41$ (not shown on Fig. 3) and the system no longer converges to a dynamic steady state, and the vertical static equilibrium position becomes globally attracting. This occurs because it is no longer possible for $|\dot{w}(1, t)|$ to exceed v_{cr} , so the kick is never activated.

We conclude this section by noting that, in contrast with the experimental system, quasiperiodic solutions were not found in our simulations, indicating that the frequencies of all periodic modal responses were always rationally related. It is at least conceivable that, for other parameter choices, solutions with incommensurate frequencies may be possible, so that quasiperiodic steady states could be achieved, however, further exploration in this direction was not attempted for this study.

4 Model reduction procedure

Our model reduction procedure starts by applying the proper orthogonal decomposition (POD) to continuous displacement field data $w(x, t)$. POD finds the basis functions $\psi(x)$ such that the time-averaged projection error of w onto ψ is minimized [3, 59] :

$$\min_{\psi_i \in L^2(\Omega)} \left\langle \left\| w(x, t) - \sum_{i=1}^P (w(x, t), \psi_i) \psi_i \right\|^2 \right\rangle, \quad (15)$$

in which angle brackets $\langle \cdot \rangle$ denote the time averaging operation, $\Omega = [0, 1]$, and the objective function is subjected to the normality constraint $\|\psi\| = 1$.

It can be shown [59] that the above minimization problem is equivalent to the following infinite-dimensional eigenvalue problem:

$$\int_{\Omega} r(x, y) \psi(y) dy = \lambda \psi(x), \quad (16)$$

where the integral kernel $r(x, y)$ is the spatial correlation function for $x, y \in \Omega$:

$$r(x, y) = \langle w(x, t) w(y, t) \rangle. \quad (17)$$

Solving the eigenvalue problem Eq. (16) leads to an infinite set of eigenfunctions $\{\psi_i\}_{i=1}^{\infty}$, in this case referred to as proper orthogonal modes (POMs), each with a corresponding eigenvalue λ_i that denotes the variance of $w(x, t)$ along $\psi_i(x)$. The POMs are sorted based on the magnitudes of the associated λ_i , and the first P of these modes are chosen to form a P -dimensional subspace, onto which the governing equation of the system is projected. The model reduction problem then becomes essentially that of identifying a “good” value of P .

For the current problem, the displacement and velocity data obtained from simulations of the hybrid system described by models A, B, and C (Eqs. 4 and 5), were discretely sampled and collected in matrices $\mathbf{W}, \dot{\mathbf{W}} \in \mathbb{R}^{N_{\Omega} \times N_t}$ such that

$$W_{ij} = w(x_i, t_j) \quad (18a)$$

$$\dot{W}_{ij} = \dot{w}(x_i, t_j), \quad (18b)$$

where N_{Ω} and N_t denote the number of discrete measurements in the spatial and temporal domains, respectively. Thus, the correlation kernel $r(x, y)$ of Eq. (17) becomes the matrix

$$\mathbf{R} = \frac{1}{N_t} \mathbf{W} \mathbf{W}^T \in \mathbb{R}^{N_{\Omega} \times N_{\Omega}}, \quad (19)$$

in which trapezoidal integration is used to approximate the time-average [60]. Eigenvectors $\boldsymbol{\Psi} \in \mathbb{R}^{N_{\Omega} \times 1}$ from the matrix eigenvalue problem

$$\mathbf{R} \boldsymbol{\Psi} = \lambda \boldsymbol{\Psi} \quad (20)$$

are then interpolated using Chebychev polynomials to yield functions $\widehat{\psi}(x)$ continuous in x that approximate the eigenfunctions $\psi(x)$ (that is, the POMs) in Eq. (16). The displacement field is then approximated by a Ritz expansion using the POMs:

$$w(x, t) \approx \widehat{w}(x, t) = \sum_{j=1}^P b_j(t) \widehat{\psi}_j(x). \quad (21)$$

The data used for the above calculations was collected as the system traversed all 8 regions in the phase space (Fig. 2). We thus obtain one set of POMs for the entire hybrid phase space: these will be used to construct a P -dimensional piecewise linear ROM. Having a global set of POMs obviates the need to separately ensure continuity for the displacement and velocity fields across transition boundaries using different basis functions, as was necessary during simulations via Eqs. (12) and (13).

Substituting the expansion Eq. (21) in terms of the POMs into the weak form of the system's governing equations, Eqs. (4) and (5), and performing a Galerkin projection on the residual, we obtain a P -dimensional system of second order ODEs for each of models A, B, and C. For example, consider model C, for which the boundary conditions Eq. (5c) contain both inertial and restoring forces. These yield the following set of P coupled ordinary differential equations (ODEs) in terms of the proper orthogonal coordinates $b_j(t)$:

$$\begin{aligned} \sum_{i=1}^P \left\{ \ddot{b}_i(t) \int_0^1 \widehat{\psi}_i(x) \widehat{\psi}_j(x) dx + b_i(t) \int \widehat{\psi}_i''(x) \widehat{\psi}_j''(x) dx + c_v \dot{b}_i(t) \int_0^1 \widehat{\psi}_i(x) \widehat{\psi}_j(x) dx \right. \\ \left. + c_m \dot{b}_i(t) \int \widehat{\psi}_i''(x) \widehat{\psi}_j''(x) dx + (k b_i(t) + m \dot{b}_i(t)) \widehat{\psi}_i(1) \widehat{\psi}_j(1) \right\} = 0 \\ \implies \sum_{i=1}^P \left\{ [M_{ij} + m E_{ij}] \ddot{b}_i(t) + [M_{ij} c_v + c_m K_{ij}] \dot{b}_i(t) + [K_{ij} + k E_{ij}] b_i(t) \right\} = 0, \quad (22) \end{aligned}$$

where

$$M_{ij} = \int_0^1 \widehat{\psi}_i(x) \widehat{\psi}_j(x) dx \quad \text{and} \quad K_{ij} = \int_0^1 \widehat{\psi}_i''(x) \widehat{\psi}_j''(x) dx \quad (23)$$

are the main elements of the mass and stiffness matrices, respectively, and

$$E_{ij} = \widehat{\psi}_i(1) \widehat{\psi}_j(1) \quad (24)$$

are elements of a coupling matrix arising from the boundary condition at $x = 1$: examination of Eq. (22) indicates that this boundary coupling also contributes to the ROM's overall mass and stiffness properties. Note that, like the original system, the ROM does not have proportional damping, so it also fails to be diagonalizable. Similar calculations yield systems of ODEs for models A and B.

To this point, our procedure has employed a relatively straightforward implementation of standard POD; we now select the dimension P of the reduced order model (ROM) using the energy closure criterion [3, 4], summarized briefly here.

P is chosen to ensure that the subspace spanning $\{\widehat{\psi}_i(x)\}_{i=1}^P$ is closed with respect to energy flowing in and out of it, to within a specified numerical tolerance. This approach provides a physics-based explanation for why a given dimension is needed in a way that mere examination of the total variance cannot.

In this case, the dissipation energy (or work), W_d , and input energy (or work), W_f , for the full-order system over one period T of a steady-state periodic response are given by

$$W_f = \int_0^T F \dot{w}(1, t) dt \quad \text{and} \quad (25a)$$

$$W_d = c_v \int_0^1 \int_0^T \dot{w}^2(x, t) dt dx + c_m \int_0^1 \int_0^T \dot{w}''^2(x, t) dt dx, \quad (25b)$$

where F is the state-dependent kick strength, as defined in Sec. 2 and summarized in Fig. 2. At steady-state, W_d and W_f must be in balance:

$$W_d = W_f. \quad (26)$$

To check whether this is the case on a subspace of dimension P , we estimate them using the P -dimensional projection of the original velocity data and its spatial derivatives in Eqs. (25). We write these estimates as \widetilde{W}_d and \widetilde{W}_f , respectively. For an insufficiently large value of P , \widetilde{W}_d and \widetilde{W}_f will not be in balance.

The projection of the discrete velocity field stored in the matrix \dot{W} (Eq. 18b) is given by

$$\widetilde{\dot{W}} = \boldsymbol{\Psi} \boldsymbol{\Psi}^T \dot{W} \quad (27)$$

where $\boldsymbol{\Psi} \in \mathbb{R}^{N_\Omega \times P}$ are the eigenvectors found from the matrix eigenvalue problem Eq. (20). To reduce discretization errors in the work estimates \widetilde{W}_d and \widetilde{W}_f , which depend on the velocity and strain rate fields (Eq. 25), we interpolated each column of $\widetilde{\dot{W}}$, representing the spatial component of the velocity data at every time sample, using Chebychev polynomials, as was done to interpolate the POMs. This ensured lower error in the estimates of the second order spatial derivative required for Eq. (25b). The time integrations needed for both energy estimates Eq. (25) were performed using the trapezoidal rule; the spatial integrations were numerically evaluated using the Chebyshev polynomial representation [61].

Given \widetilde{W}_d and \widetilde{W}_f , we define the energy convergence errors [4],

$$e_f = \left| 1 - \frac{\widetilde{W}_f}{\widetilde{W}_f^{P_{\max}}} \right| \quad \text{and} \quad e_d = \left| 1 - \frac{\widetilde{W}_d}{\widetilde{W}_d^{P_{\max}}} \right|, \quad (28)$$

of the input and dissipation energy, respectively: both e_d and e_f are functions of P . In these expressions, the superscript P_{\max} indicates the energy value estimated at $P = P_{\max}$, where P_{\max} is the numerically estimated rank of \mathbf{R} (Eq. 19). POMs for $P > \text{rank}(\mathbf{R})$ lie in the null space of \mathbf{R} and do not capture the system's dynamics [3]. Hence, P_{\max} indicates the maximum ROM dimension that a given data set is capable of capturing. Once \widetilde{W}_f and \widetilde{W}_d are captured with sufficient accuracy, physics *requires* that they approximately balance each other. Thus, the value of the subspace dimension P for which e_f and e_d drop below a given predefined tolerance ϵ_{tol} , is selected as the ROM dimension.

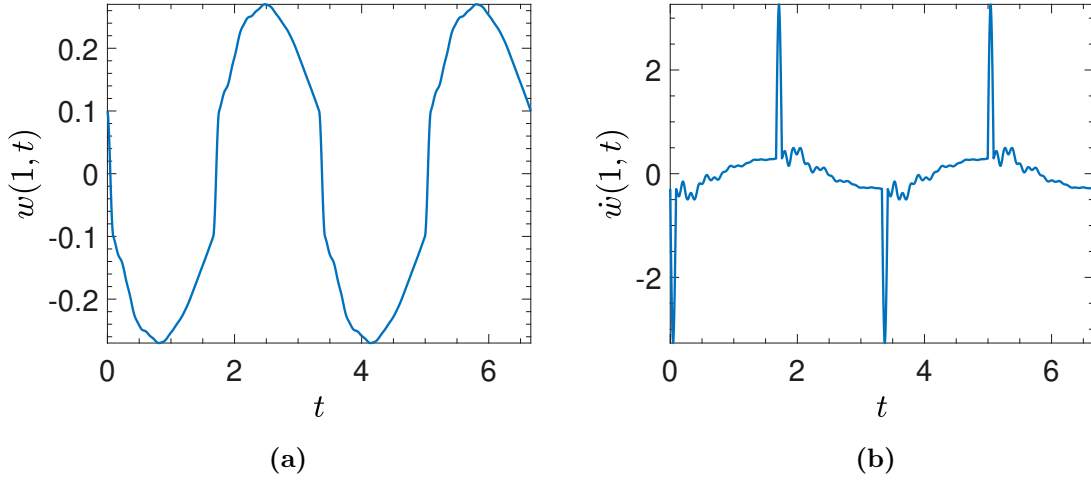


Figure 5: Period-1, steady-state (a) displacement and (b) velocity time-series of the full order system, at the beam tip ($x = 1$). The beam is subjected to a kick strength $F \approx 12.95$. The fundamental period of the time-series is $T \approx 3.25$ units. The remaining parameter values are same as in Fig. 3.

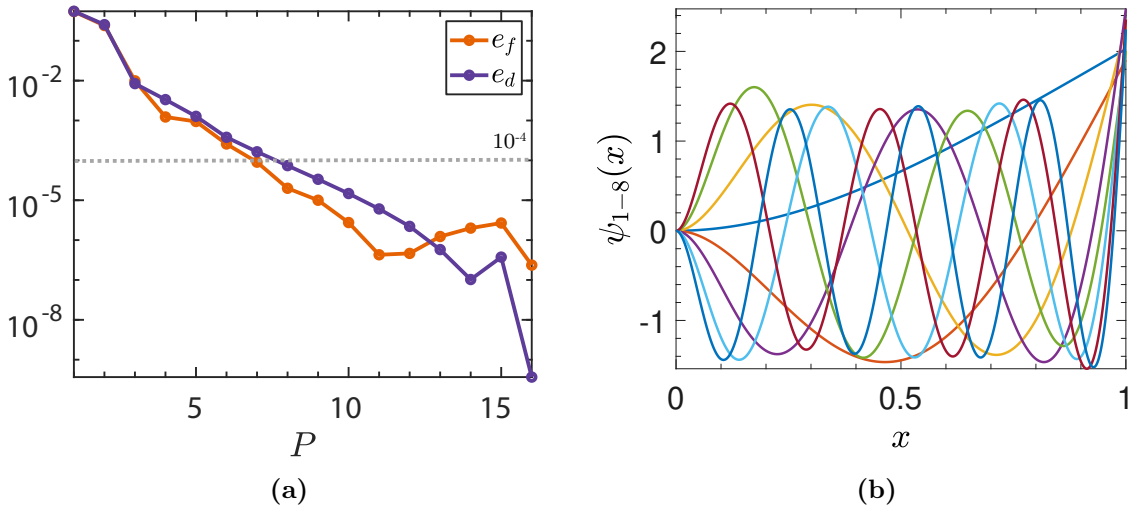


Figure 6: Energy closure analysis for the period-1 solution of Fig. 5: (a) The energy convergence errors e_d and e_f (Eq. 28) vs. subspace dimension P . Both curves decrease below the tolerance $\epsilon_{\text{tol}} = 10^{-4}$ at $P = 8$. (b) The corresponding eight POMs that span the subspace, obtained by applying POD on the displacement data.

5 Results

Out of the wide variety of steady-state responses shown Fig. 3, we first selected the period-1 solution corresponding to $F \approx 12.95$ (see Fig. 4a) to perform model reduction. Representative displacement and velocity time series are shown in Fig. 5. We selected the dimension of the ROM using the energy closure criterion: in Fig. 6a, we plot both e_d and e_f against P and observe that both decrease in a monotonic fashion. This indicates that \widetilde{W}_d and \widetilde{W}_f converge to their true values, W_d and W_f , respectively, which further suggests that the subspaces have come into energy balance. In this case, after initial experimentation, we selected $\epsilon_{\text{tol}} = 10^{-4}$. For $P \geq 8$, both e_d and e_f fall below this tolerance, indicating approximate energy closure, so we formulated an 8 DOF ROM following the steps described in the previous section. The corresponding 8 POMs, which globally span the subspaces for ROMs in all regions of the hybrid system’s phase space, are shown in Fig. 6b. We remark that these empirical shape functions approximate the normal modes for a clamped-free beam, despite the more complex piecewise boundary conditions: this likely indicates that the system typically spends relatively little time with the tip interacting with the electromagnet or its core. Furthermore, we note that the maximum possible ROM dimension obtainable with from the data set, $P_{\text{max}} = 16$, indicated by the upper limit of the horizontal axis in Fig. 6a, was determined from the rank of the displacement covariance matrix Eq. (19). Thus, the ROM dimension that achieves energy closure is well below the resolving power of the data set. For the sake of comparison, we also applied the conventional variance-based mode-selection criterion, which showed that $P = 3$ dimensions were needed to capture 99.9% of the total response variance.

In Fig. 7, we use phase plane plots at the beam’s midpoint and tip to contrast the dynamics of the full order system (FOS) against the 3 DOF ROM, formulated using a total variance criterion, and the 8 DOF ROM, formulated using the energy closure criterion (Figs. 7a and 7b, respectively). Upon inspecting both figures, it is clear that the 3 DOF ROM struggles to accurately reflect the period-1 dynamics exhibited by the FOS. The root mean square (RMS) errors for the displacement and velocity fields (that is, along the length of the beam) were computed for the 3 DOF ROM and found to be approximately 35.4% and 114.7%, respectively. In contrast, the performance of the phase plane orbits at both locations for the 8 DOF ROM mirror that of the full order system with high fidelity, as reflected by the fact that the RMS errors for the displacement and velocity fields were 0.002% and 0.2%, respectively.

The same outcome is observed while comparing power spectra of the displacement and velocity time series of the FOS and the ROMs using the beam tip time series, as shown in Fig. 8. The fundamental frequency of the response of the FOS, shown in purple, is approximately 0.307, corresponding to a fundamental period $T \approx 3.25$, as can also be seen in the time series plots of Fig. 5. The other peaks are at odd harmonics of the fundamental frequency. From Figs. 8a and 8b we see the frequency content of the response obtained from the 8 DOF ROM is nearly identical to the FOS: all peaks in the frequency domain are almost perfectly aligned with those of the FOS as shown by the red line, indicating high accuracy of the ROM in capturing different time scales of the FOS response. In contrast,

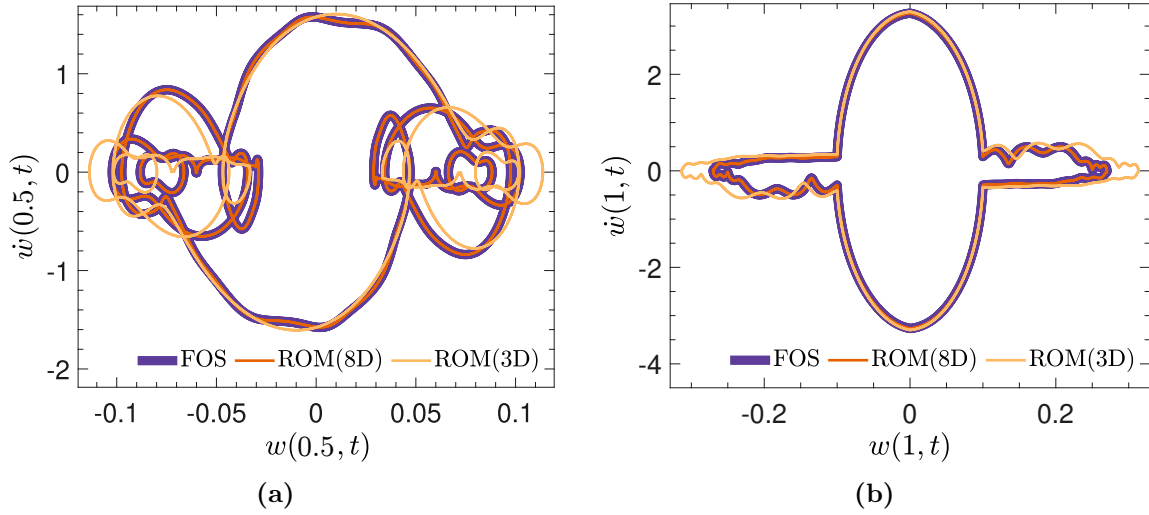
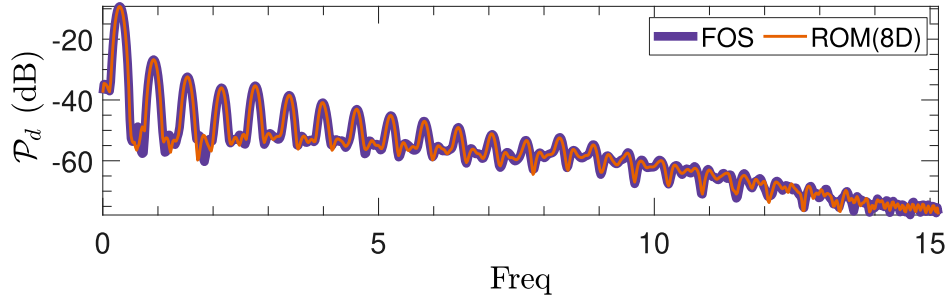


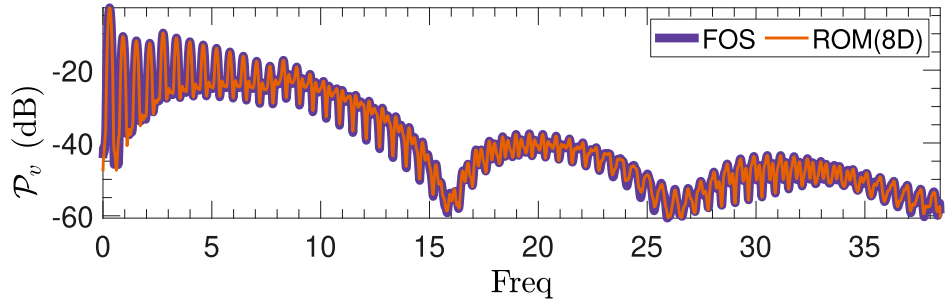
Figure 7: Phase plane plots illustrating the accuracy of reduced order models (ROMs) of the kicked oscillator, obtained by applying proper orthogonal decomposition (POD) to displacement data from period-1 solution of Figs. 4a and 5, with ROM dimensions P selected with energy closure criterion and variance-based criterion using 99.9% of total variance. Energy closure gives $P = 8$, while the variance-based criterion gives $P = 3$. (a) Comparison of ROM responses to that of full order system (FOS) at $x = 0.5$. (b) Same comparison at $x = 1$. At both locations, the 3 DOF ROM fails to approximate the response of the FOS (relative displacement and velocity field errors: 35.35% and 114.71%, respectively); 8 DOF ROM response is virtually identical to that of the FOS (relative displacement and velocity field errors: 0.002% and 0.2%, respectively).

if we compare the frequency content of the response from the 3 DOF ROM, as shown in Figs. 8c and 8d, we observe that the overall structure of the power spectrum is significantly different and even though the first five or six frequency peaks align with those of the FOS, the peaks at higher frequencies diverge substantially. Thus, the 8 DOF ROM formulated using the energy closure criterion clearly outperforms the 3 DOF ROM formulated based on the mode selection based on 99.9% of the total variance. Now, obviously, one can try increasing the fraction of total variance to formulate a ROM with comparable accuracy; however, the point here is that energy-closure provides a physically grounded explanation as to *why* the additional modes are required.

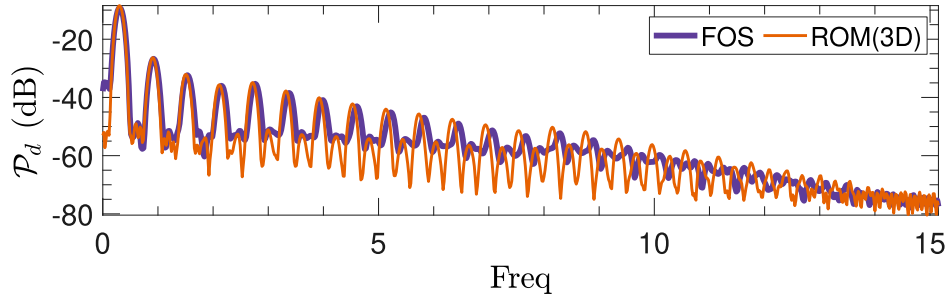
A major open question when creating ROMs in nonlinear systems is how robust they are with respect to changes in parameters, particularly across bifurcations. We examined if the 8 DOF ROM formulated above, which is based only on period-1 solution data for $F = 12.95$, can accurately approximate other steady-state responses of the FOS corresponding for other values of F . To this end, we attempted to reconstruct the bifurcation diagram of Fig. 3 using the 8 DOF ROM. The result is shown in Fig. 9, in which we see that the 8 DOF ROM is capable of recovering the complete bifurcation structure found using the full order system (FOS).



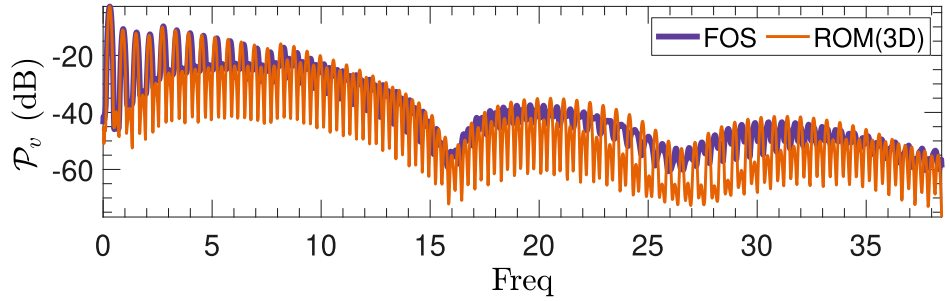
(a)



(b)



(c)



(d)

Figure 8: Comparison of the power spectra for the full order system (FOS) and 8 DOF ROM: (a) displacement and (b) velocity at the beam tip. Power spectra comparison between FOS and 3 DOF ROM: (c) displacement and (d) velocity time-series at the beam tip. Time series are from the solutions of Fig. 7b.

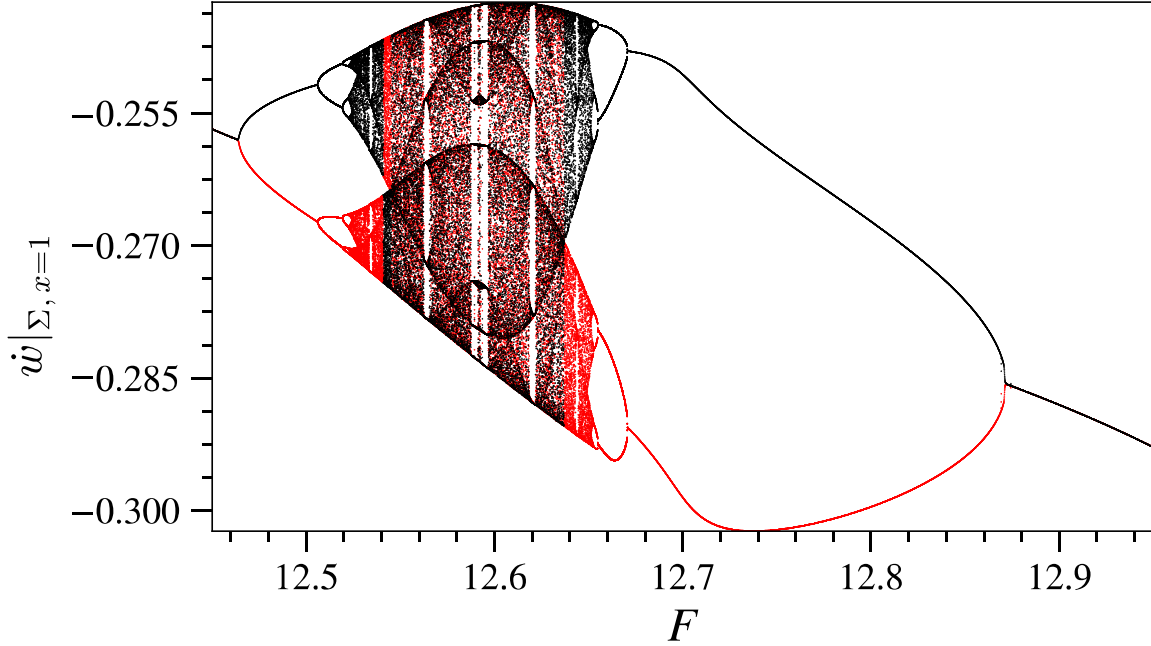


Figure 9: Reconstructed bifurcation diagram of the kicked oscillator (Fig. 3), in this case using simulations of an 8 DOF reduced order model (ROM) for kick strengths $F \in [12.44, 12.95]$. The ROM was constructed with proper orthogonal decomposition (POD) and energy closure using only displacement data from the period-1 solution at $F = 12.95$ (Fig. 4a). Despite this limited data set, the reconstructed diagram is virtually identical to the bifurcation diagram of the full order system (FOS).

To further study the robustness of our model reduction procedure, we used POD and energy closure analysis to construct different subspaces for each of each of the 10^4 solutions represented in Fig. 3. Using the same energy closure tolerance, $\epsilon_{\text{tol}} = 10^{-4}$, all subspace dimensions were found to be $P = 8$. We further checked the angles between each of these 8-dimensional subspaces: in all cases, these were found to be negligible, on the order of 10^{-3} radians. This implies that these subspaces, to within numerical error, essentially defined the same hyperplane, further implying that the different sets of POMs spanning these subspaces were at most rotations of each other. These results help explain why the original 8 DOF ROM formulated using $F = 12.95$ data was capable of recovering the full bifurcation diagram for the system. Furthermore, they strongly suggest that ROMs formulated using data from any of point in the bifurcation diagram would be able to do the same. Thus, we found that the reduced order modeling procedure is strongly robust to changes in the kick strength F .

Though the robustness of the ROM under bifurcations was not anticipated by the authors in this case, a similar phenomenon has been observed in studies of the bifurcation structure of the complex Ginzburg-Landau equation [62–64]. In these studies, it was found that POMs calculated for specific values of the bifurcation parameter could be used to simulate the system with other parameter values, as long as a sufficient number of POMs were retained. Furthermore, the researchers found that the corresponding ROMs could be expected to

show robustness in some neighborhood of the bifurcation parameter, and were able to approximate the different attractors of the system. In our study, we observe that energy closure captures a set of empirical modes that captures the dynamics in the *entire* parameter range of interest. Furthermore, the robustness of the ROMs observed in our system is an important addition to the previously reported instances in the context of fluid systems.

We conclude this section by mentioning that we also attempted to reconstruct the bifurcation diagram using the 3 DOF ROM generated using 99.9% of the total variance: we found that the resulting diagram differed substantially from Fig. 3. Thus, our results suggest that the robust construction of ROMs requires the inclusion of a sufficient number of DOF across the entire parameter range of interest and, furthermore, that these DOF should lie in the same subspace. Our study shows that energy closure analysis provides a physics-based criterion capable of doing precisely this.

6 Summary and conclusions

In this study, we have investigated the dynamics of a kicked, piecewise linear, globally nonlinear flexible oscillator, together with its model reduction using proper orthogonal decomposition (POD) with energy closure dimension estimation [3, 4]. For this paper, the physical experimental system on which our study is based, voltage-controlled kicks induce various nonlinear dynamic behaviors in the system, including periodic, quasi-periodic, and chaotic steady states. The physical magneto-mechanical oscillator is modeled as a Bernoulli-Euler beam with a point mass at its tip, which can be kicked by a position-triggered constant force of adjustable strength. The overall nonlinear infinite-dimensional hybrid system is defined by how the piecewise kicking force creates 8 regions in the system’s phase space (Fig. 2), resulting in 3 distinct linear models, each with its own boundary conditions (Eqs. 4 and 5). For numerical experiments, we approximated the system’s dynamics using a 25 degree of freedom (DOF) linear model in each phase space region, which enabled us to perform high-fidelity simulations under varying kick strengths. The system’s responses were subsequently summarized with a bifurcation diagram using the kick strength F as a bifurcation parameter (Fig. 3): we found a complex bifurcation structure including a diversity of periodic and chaotic steady states.

We derived a reduced order model (ROM) using displacement field data for a period-1 steady state at $F = 12.95$, finding an 8 degree of freedom (DOF) model that satisfied energy closure to within a specified tolerance. These ROMs not only accurately captured the corresponding dynamics of the full order system, but also significantly improved computational speed, by approximately 300%. More remarkably, the ROM estimated for this particular response was capable of recovering the entire bifurcation structure of the system (Fig. 9). This robustness is arguably most surprising given that our system is subjected to impulsive loading discontinuities and, hence, can be expected to excite a large number of modes across boundaries of the hybrid system and, perhaps, to have more complex, nonsmooth bifurcations. However, POD, together with a fixed energy closure tolerance, was found to select subspaces of the same dimension and spanning nearly identical hyperplanes across

the entire range of the bifurcation parameter F .

In contrast, a 3 DOF ROM, whose dimension was estimated for the same data set using a conventional criterion of capturing 99.9% of the total variance, failed to accurately replicate the true response or, therefore perhaps obviously, the bifurcation diagram. While it is, of course, true that one can simply raise the fraction of total variance used (to 99.99%, 99.999%, etc.) to include more DOF for a ROM, such a purely statistical approach is inferior to energy closure in at least two ways. First, energy closure provides a physics-based explanation for *why* a specific number of empirical modes needs to be included in a specific instance. From the perspective of energy closure, the relative amplitude of a given mode is not as important as its energetic role: it is quite conceivable that a DOF with relatively small variance might nevertheless be crucial to balancing energy. Second, it is not uncommon for different levels of variance to be required to accurately model different steady states in the same system, whereas, at least for this system, the same energy closure tolerance provided accurate ROMs *and* accurately captured the system’s bifurcation structure. This suggests that the degree of energy closure provides a *uniform* bound on ROM performance in a way that total variance does not.

This study has demonstrated the effectiveness of energy closure analysis for model order reduction. Indeed, the application of energy closure to this piecewise linear, globally nonlinear system was able to overcome limitations encountered in earlier studies of the dimensionality of nonsmooth systems based on POD [5, 6]. To the best of our knowledge, this is the first successful model reduction of a high-dimensional, nonsmooth, structural system carried out to date. POD is most commonly applied, at least in the physical sciences and engineering, in situations where first-principles models are available for reduction; however, in principle it can be applied to data-driven models. However, as presented here, energy closure itself clearly requires first-principles models of system energetics (e.g., as in Eq. 25). For more complex and/or unusual dynamical systems, for which such models may not be readily available or even defined, energy closure based model reduction may not be applicable. Nevertheless, this may be possible in the future: contemporary research on data-driven reduced order modeling techniques with physics-informed neural networks aim to achieve this. Given that such methods require solving an optimization problem for model estimation, similar to POD, it may in the future be feasible to incorporate energy closure analysis directly into the loss function of the optimization problem. Such integration represents a promising direction for future research.

Given the purely analytical and numerical in nature of this work, our model reduction analysis was able to make use of full-state field data. Even when complete first-principles models are available, model reduction using insufficient and/or highly noisy experimental data alone may obstruct the accurate estimation of energy closure. In [4], we provided details on how to manage situations where experimental data is insufficient for estimating energy closure, such as when only displacement data is available and velocity data is not. We also discussed strategies to reduce measurement noise and efficient methods to calculate energy closure with noisy data.

As implemented here, energy closure analysis exploited the periodicity of solutions to facili-

tate calculations, in that energy input and dissipated (Eq. 25) needed only to be computed using data from one steady-state response period. However, our approach is not limited to the analysis of periodic response data: in principle, chaotic, or even random, behaviors can be analyzed for energy closure with, however, the likely expense of having to collect more data to accurately estimate the *average* energy balance. Indeed, this was what was done to determine the consistency of subspaces obtained using data from each of the 10^4 values of F of Fig. 3: to quantify energy closure for the chaotic responses, we used the data from all 16 forcing periods used to construct the bifurcation diagram, and found that this was sufficient to attain statistical convergence. All this said, however, at least for deterministic systems, a very important practical consequence of the robustness of the ROMs demonstrated in our study is that only data from periodic responses need be studied. This provides a potentially massive savings in the time required for data collection.

References

- [1] L. Sirovich, “Turbulence and the dynamics of coherent structures I: Coherent structures,” *Quarterly of Applied Mathematics*, vol. 45, no. 3, pp. 561–571, 1987.
- [2] G. Berkooz, P. Holmes, and J. L. Lumley, “The proper orthogonal decomposition in the analysis of turbulent flows,” *Annual Review of Fluid Mechanics*, vol. 25, no. 1, pp. 539–575, 1993.
- [3] S. Bhattacharyya and J. P. Cusumano, “An energy closure criterion for model reduction of a kicked Euler-Bernoulli beam,” *Journal of Vibration and Acoustics*, vol. 143, Nov 2020.
- [4] S. Bhattacharyya and J. P. Cusumano, “Experimental implementation of energy closure analysis for reduced order modeling,” *Journal of Vibration and Acoustics*, vol. 144, 05 2022. 051007.
- [5] J. P. Cusumano and B. Y. Bai, “Period-infinity periodic motions, chaos, and spatial coherence in a 10 degree of freedom impact oscillator,” *Chaos, Solitons & Fractals*, vol. 3, no. 5, pp. 515–535, 1993.
- [6] J. P. Cusumano, M. T. Sharkady, and B. W. Kimble, “Experimental measurements of dimensionality and spatial coherence in the dynamics of a flexible-beam impact oscillator,” *Philosophical Transactions: Physical Sciences and Engineering*, vol. 347, no. 1683, pp. 421–438, 1994.
- [7] S. Chatterjee, A. Mallik, and A. Ghosh, “Periodic response of piecewise non-linear oscillators under harmonic excitation,” *Journal of Sound and Vibration*, vol. 191, pp. 129–144, Mar. 1996.
- [8] M. Wiercigroch and V. W. T. Sin, “Experimental study of a symmetrical piecewise base-excited oscillator,” *Journal of Applied Mechanics*, vol. 65, pp. 657–663, Sept. 1998.

- [9] P. Blankeship and F. Kahraman, “Steady state forced response of a mechanical oscillator with combined parametric excitation and clearance type non-linearity,” *Journal of Sound and Vibration*, vol. 185, no. 5, pp. 743–765, 1995.
- [10] F. F. Ehrich, “Observations of subcritical superharmonic and chaotic responses,” *ASME Journal of Vibration and Acoustics*, vol. 114, pp. 93–100, 1992.
- [11] H. D. Gonsalves, R. D. Neilson, and A. D. S. Barr, “A study of the response of a discontinuously nonlinear rotor system,” *Nonlinear Dynamics*, vol. 7, pp. 451–470, 1995.
- [12] F. C. Moon and S. W. Shaw, “Chaotic vibrations of a beam with non-linear boundary conditions,” *International Journal of Non-Linear Mechanics*, vol. 18, pp. 465–477, 1983.
- [13] S. Natsiavas, “Periodic response and stability of oscillators with symmetric trilinear restoring force,” *Journal of Sound and Vibration*, vol. 134, no. 2, pp. 313–331, 1989.
- [14] A. B. Nordmark, “Non-periodic motion caused by grazing incidence in an impact oscillator,” *Journal of Sound and Vibration*, vol. 145, no. 2, pp. 279–287, 1991.
- [15] F. Peterka and J. Vacik, “Transition to chaotic motion in mechanical systems with impacts,” *Journal of Sound and Vibration*, vol. 154, no. 1, pp. 95–115, 1992.
- [16] S. W. Shaw and P. J. Holmes, “A periodically forced piecewise linear oscillator,” *Journal of Sound and Vibration*, vol. 90, no. 1, pp. 129–155, 1983.
- [17] S. W. Shaw, “Forced vibrations of a beam with one-sided amplitude constraint: Theory and experiment,” *Journal of Sound and Vibration*, vol. 99, no. 2, pp. 199–212, 1985.
- [18] W. T. V. Sin and M. Wiercigroch, “Experimental and numerical study of a symmetrically piecewise linear oscillator,” in *Proceedings of the ASME Elasto-Impact and Friction in Dynamic Systems*, vol. DE-Vol. 90, pp. 63–68, 1996.
- [19] A. Stenson and A. B. Nordmark, “Experimental investigations of some consequences of low impacts in the chaotic dynamics of mechanical systems,” *Philosophical Transactions of the Royal Society of London, Series A: Mathematical, Physical and Engineering Sciences*, vol. 347, pp. 439–448, 1994.
- [20] T. Watanabe, “Forced vibrations of continuous system with nonlinear boundary conditions,” *ASME Journal of Mechanical Design*, vol. 100, pp. 487–491, 1974.
- [21] M. Wiercigroch, “Bifurcation analysis of harmonically excited linear oscillator with clearance,” *Chaos, Solitons and Fractals*, vol. 4, no. 2, pp. 297–303, 1994.
- [22] M. Wiercigroch, *Dynamics of Discrete Mechanical Systems with Discontinuities*. Gliwice: Silesian University Press, 1994.
- [23] M. Wiercigroch, “On modelling discontinuities in dynamic systems,” *Machine Vibration*, vol. 5, pp. 112–119, 1996.

- [24] H. Hu, “Detection of grazing orbits and incident bifurcations of a forced continuous, piecewise-linear oscillator,” *Journal of Sound and Vibration*, vol. 187, pp. 485–493, Nov. 1995.
- [25] Z. Ming-Xin, W. Jun, S. Yong-Jun, and Z. Jian-Chao, “Analytical threshold for chaos of piecewise duffing oscillator with time-delayed displacement feedback,” *Shock and Vibration*, vol. 2022, pp. 1–11, Mar. 2022.
- [26] J. P. Cusumano, “Nonlinear modal interactions and low order modeling of a kicked flexible rod,” *Proceedings in Applied Mathematics and Mechanics*, vol. 7, no. 1, pp. 1030305–1030306, 2007.
- [27] J. P. Cusumano, “Experimental application of the Karhunen-Loève decomposition to the study of modal interactions in a mechanical oscillator,” in *AIP Conference Proceedings: Chaotic, fractal, and nonlinear signal processing*, vol. 375, pp. 446–458, AIP, 1996.
- [28] N. Franco, A. Manzoni, and P. Zunino, “A deep learning approach to reduced order modelling of parameter dependent partial differential equations,” *Mathematics of Computation*, vol. 92, pp. 483–524, 2023.
- [29] R. Maulik, A. Mohan, B. Lusch, S. Madireddy, P. Balaprakash, and D. Livescu, “Time-series learning of latent-space dynamics for reduced-order model closure,” *Physica D: Nonlinear Phenomena*, vol. 405, p. 132368, Apr. 2020.
- [30] W. D. Fries, X. He, and Y. Choi, “LaSDI: Parametric latent space dynamics identification,” *Computer Methods in Applied Mechanics and Engineering*, vol. 399, p. 115436, Sept. 2022.
- [31] X. He, Y. Choi, W. D. Fries, J. L. Belof, and J.-S. Chen, “gLaSDI: Parametric physics-informed greedy latent space dynamics identification,” *Journal of Computational Physics*, vol. 489, p. 112267, Sept. 2023.
- [32] S. L. Brunton, J. L. Proctor, and J. N. Kutz, “Discovering governing equations from data by sparse identification of nonlinear dynamical systems,” *Proceedings of the National Academy of Sciences*, vol. 113, pp. 3932–3937, Mar 2016.
- [33] B. Daniels and I. Nemenman, “Automated adaptive inference of phenomenological dynamical models,” *Nature Communications*, vol. 6, p. 8133, 2015.
- [34] S. Atkinson, “Bayesian hidden physics models: uncertainty quantification for discovery of nonlinear partial differential operators from data,” *arXiv e-prints*, 2020. arXiv:2006.04228.
- [35] H. Ribera, S. Shirman, A. Nguyen, and N. Mangan, “Model selection of chaotic systems from data with hidden variables using sparse data assimilation,” *Chaos*, vol. 32, p. 063101, 2022.

- [36] S. Fresca and A. Manzoni, “POD-DL-ROM: Enhancing deep learning-based reduced order models for nonlinear parametrized PDEs by proper orthogonal decomposition,” *Computer Methods in Applied Mechanics and Engineering*, vol. 388, p. 114181, 2022.
- [37] B. Feeny, “On proper orthogonal co-ordinates as indicators of modal activity,” *Journal of Sound and Vibration*, vol. 255, no. 5, pp. 805–817, 2002.
- [38] D. Chelidze and W. Zhou, “Smooth orthogonal decomposition-based vibration mode identification,” *Journal of Sound and Vibration*, vol. 292, no. 3-5, pp. 461–473, 2006.
- [39] B. F. Feeny and R. Kappagantu, “On the physical interpretation of proper orthogonal modes in vibrations,” *Journal of Sound and Vibration*, vol. 211, no. 4, pp. 607–616, 1998.
- [40] E. Shlizerman, E. Ding, M. O. Williams, and J. N. Kutz, “The proper orthogonal decomposition for dimensionality reduction in mode-locked lasers and optical systems,” *International Journal of Optics*, vol. 2012, pp. 1–18, 2012.
- [41] L. Sirovich, “Chaotic dynamics of coherent structures,” *Physica D: Nonlinear Phenomena*, vol. 37, no. 1, pp. 126–145, 1989.
- [42] M. Azeez and A. Vakakis, “Proper orthogonal decomposition (POD) of a class of vibroimpact oscillations,” *Journal of Sound and Vibration*, vol. 240, no. 5, pp. 859–889, 2001.
- [43] G. Kerschen, J.-C. Golinval, A. F. Vakakis, and L. A. Bergman, “The method of proper orthogonal decomposition for dynamical characterization and order reduction of mechanical systems: An overview,” *Nonlinear dynamics*, vol. 41, no. 1-3, pp. 147–169, 2005.
- [44] T. Kostova-Vassilevska and G. M. Oxberry, “Model reduction of dynamical systems by proper orthogonal decomposition: Error bounds and comparison of methods using snapshots from the solution and the time derivatives,” *Journal of Computational and Applied Mathematics*, vol. 330, pp. 553–573, 2018.
- [45] Y. Jin, K. Lu, L. Hou, and Y. Chen, “An adaptive proper orthogonal decomposition method for model order reduction of multi-disc rotor system,” *Journal of Sound and Vibration*, vol. 411, pp. 210–231, 2017.
- [46] S. Bellizzi and R. Sampaio, “Karhunen-Loève modes obtained from displacement and velocity fields: Assessments and comparisons,” *Mechanical Systems and Signal Processing*, vol. 23, no. 4, pp. 1218–1222, 2009.
- [47] S. Bellizzi and R. Sampaio, “Smooth Karhunen-Loève decomposition to analyze randomly vibrating systems,” *Journal of Sound and Vibration*, vol. 325, no. 3, pp. 491–498, 2009.
- [48] K. S. Breuer and L. Sirovich, “The use of the Karhunen-Loève procedure for the calculation of linear eigenfunctions,” *Journal of Computational Physics*, vol. 96, no. 2, pp. 277–296, 1991.

- [49] R. Everson and L. Sirovich, “Karhunen-Loève procedure for gappy data,” *JOSA A*, vol. 12, no. 8, pp. 1657–1664, 1995.
- [50] A. J. Newman, “Model reduction via the Karhunen-Loève expansion part I: An exposition,” Tech. Rep. T.R. 96-32, Institute for Systems Research, University of Maryland, 1996.
- [51] A. J. Newman, “Model reduction via the Karhunen-Loève expansion part I: An exposition,” Tech. Rep. T.R. 96-32, Institute for Systems Research, University of Maryland, 1996.
- [52] C. Wolter, M. Trindade, and R. Sampaio, “Reduced-order model for an impacting beam using the Karhunen-Loève expansion,” *TEMA - Tendências em Matemática Aplicada e Computacional*, vol. 3, no. 2, 2002.
- [53] K. S. Surana and J. N. Reddy, *The Finite Element Method for Boundary Value Problems: Mathematics and Computations*. Boca Raton: CRC Press, 1st edition ed., 2016.
- [54] T. J. R. Hughes, *The Finite Element Method: Linear Static and Dynamic Finite Element Analysis*. Mineola, NY: Dover Publications, 1 edition ed., 2000.
- [55] L. Meirovitch, *Fundamentals of Vibrations*. Boston: McGraw-Hill, 2001.
- [56] S. S. Rao, *Vibration of Continuous Systems*. John Wiley & Sons, Inc., Dec. 2006.
- [57] J. Guckenheimer and P. Holmes, *Nonlinear Oscillations, Dynamical Systems, and Bifurcations of Vector Fields*, vol. 42. New York: Springer-Verlag, 1983.
- [58] R. Seydel and R. Seydel, *Practical Bifurcation and Stability Analysis: From Equilibrium to Chaos*. No. v. 5, New York: Springer-Verlag, 2nd ed ed., 1994.
- [59] P. Holmes, G. Berkooz, and J. L. Lumley, *Turbulence, Coherent Structures, Dynamical Systems and Symmetry*. Cambridge: Cambridge University Press, 1996.
- [60] S. L. Brunton and J. N. Kutz, *Data-Driven Science and Engineering*. Cambridge University Press, Jan 2019.
- [61] T. A. Driscoll, N. Hale, and L. N. Trefethen, eds., *Chebfun Guide*. Pafnuty Publications, Oxford, 2014.
- [62] F. Terragni and J. M. Vega, “Efficient computation of bifurcation diagrams via adaptive ROMs,” *Fluid Dynamics Research*, vol. 46, no. 4, p. 041412, 2014.
- [63] M. L. Rapún, F. Terragni, and J. M. Vega, “Mixing snapshots and fast time integration of PDEs,” in *Proc. IV Int. Conf. on Comput. Methods for Coupled Problems in Science and Eng* (M. Papadrakakis, E. Oñate, and B. Schrefler, eds.), no. 246 in COUPLED PROBLEMS, pp. 1–12, 2011.
- [64] F. Terragni and J. M. Vega, “On the use of POD-based ROMs to analyze bifurcations in some dissipative systems,” *Physica D: Nonlinear Phenomena*, vol. 241, pp. 1393–1405, Sept. 2012.

Appendices

A Nondimensionalization of governing equations

Implementing Hamilton's principle, the governing partial differential equation (PDE) of a cantilever Bernoulli-Euler beam of length l , with point mass m and spring to ground of stiffness k , both at the tip, as shown in Fig. 1b, can be written in *dimensioned* form as:

$$\rho A \ddot{w} + EI w'''' + c_m EI \dot{w}'''' + c_v \dot{w} = 0, \quad (29)$$

where $w(x, t)$ denotes the horizontal deflection of the beam during oscillation measured from the vertical neutral axis, with $x \in [0, l]$; primes and overdots indicate derivatives with respect to x and t , respectively; c_m and c_v denote coefficients of material damping and viscous damping, respectively; E is Young's modulus; I is the cross-sectional area moment of inertia of the beam; A is area of cross section; and ρ is the mass density of beam material.

Hamilton's principle also provides dimensioned boundary conditions. As discussed in Sec. 2.2, and summarized in Fig. 2, the system has a hybrid set of boundary conditions. For the purposes here, we need only focus on model B, corresponding to the system when the kick force is active (Eqs. 2):

$$\begin{aligned} w(0, t) &= 0 \\ w'(0, t) &= 0 \\ EI (w''(l, t) + c_m \dot{w}''(l, t)) &= 0 \\ EI (w'''(l, t) + c_m \dot{w}'''(l, t)) &= m \ddot{w}(l, t) + kw(l, t) + \text{sgn}(\dot{w}(l, t))F, \end{aligned} \quad (30)$$

To non-dimensionalize the above system, we indicate dimensionless variables by an overbar and define $x = l\bar{x}$, $w = l\bar{w}$ and $t = t_c\bar{t}$, where t_c is to be found. The differential operators then become

$$\frac{\partial}{\partial x} = \frac{1}{l} \frac{\partial}{\partial \bar{x}} \quad \text{and} \quad \frac{\partial}{\partial t} = \frac{1}{t_c} \frac{\partial}{\partial \bar{t}},$$

so Eq. (29) can be written as

$$\begin{aligned} \rho A \frac{\ddot{\bar{w}}}{t_c^2} + EI \frac{\bar{w}''''}{l^4} + c_m EI \frac{\dot{\bar{w}}''''}{l^4 t_c} + c_v \frac{\dot{\bar{w}}}{t_c} &= 0 \\ \implies \ddot{\bar{w}} + t_c^2 \frac{EI}{\rho A l^4} \bar{w}'''' + c_m t_c \frac{EI}{\rho A l^4} \dot{\bar{w}}'''' + \frac{c_v t_c}{\rho A} \dot{\bar{w}} &= 0 \end{aligned}$$

in which and overdots and primes now represent *dimensionless* derivatives. Letting $\bar{c}_m = c_m/t_c$, $\bar{c}_v = c_v t_c/(\rho A)$ and $t_c = \sqrt{\rho A l^4/(EI)}$, the PDE can be written in *dimensionless* form as

$$\ddot{\bar{w}} + \bar{w}'''' + \bar{c}_m \dot{\bar{w}}'''' + \bar{c}_v \dot{\bar{w}} = 0. \quad (31)$$

Correspondingly, the BCs take the dimensionless form

$$\begin{aligned}
\bar{w}(0, t) &= 0 \\
\bar{w}'(0, t) &= 0 \\
\bar{w}''(1, \bar{t}) + \bar{c}_m \dot{\bar{w}}''(1, \bar{t}) &= 0 \\
\bar{w}'''(1, \bar{t}) + \bar{c}_m \dot{\bar{w}}'''(1, \bar{t}) &= \bar{m} \ddot{\bar{w}}(1, \bar{t}) + \bar{k} \bar{w}(1, \bar{t}) + \text{sgn}(\dot{\bar{w}}(1, \bar{t})) \bar{F},
\end{aligned} \tag{32}$$

in which we have also rescaled the mass, spring stiffness, and kick force using $\bar{m} = m/(\rho Al)$, $\bar{k} = kl^3/(EI)$, and $\bar{F} = Fl^2/(EI)$, respectively.

After rescaling, for convenience, we *drop overbars*, which yields the dimensionless PDE and boundary conditions, Eqs. (1) and (2), presented in Sec. 2.

B Removal of force boundary condition in kicking region

As discussed in Sec. 2.2, when finding the solution for model B, the force boundary condition (BC) in the kicking region can be easily removed by expressing the displacement field $w(x, t)$ relative to the static deflection associated with the constant tip force F .

Depending on the sign of the velocity, the static deflection in this region is given by the time-independent version of Eqs. (1) and (2):

$$w''''(x) = 0$$

and

$$\begin{aligned}
w(0) &= 0 \\
w'(0) &= 0 \\
w''(1) &= 0 \\
w'''(1) &= kw(1) \pm F,
\end{aligned} \tag{33}$$

in which the sign in front of F is to be chosen depending on the sign of the tip-velocity. We write the solution to the above boundary value problem as

$$w_s(x) = \pm \frac{3F}{3+k} \left(\frac{x^2}{2} - \frac{x^3}{6} \right). \tag{34}$$

Then, defining the relative displacement $u(x, t)$ with respect to $w_s(x)$ via $w(x, t) = w_s(x) + u(x, t)$, substitution into the second BC of Eq. (2d) (corresponding to regions 4, 8) results in a BC in u identical in form to that of the third BC of Eq. (2d) (corresponding to regions 1, 3, 5, 7), as was to be shown.

C Orthonormality conditions

For the modal analysis used in the piecewise solution of Sec. 2.2, we employed orthonormality conditions Eqs. (9): we here summarize their derivation. The relevant inner products

are obtained by looking at conservative free vibrations of the dimensionless system (Sec. A) of Eqs. (1) and (2), that is, the PDE

$$w''''(x, t) + \ddot{w}(x, t) = 0, \quad (35)$$

subjected to the boundary conditions (BCs)

$$\begin{aligned} w(0, t) &= 0 \\ w'(0, t) &= 0 \\ w''(1, t) &= 0 \\ w'''(1, t) &= m\ddot{w}(1, t) + kw(1, t). \end{aligned} \quad (36)$$

Assuming a time-harmonic response, separation of variables $w(x, t) = W(x)e^{i\omega t}$ yields the differential eigenvalue problem

$$W''''(x) - \omega^2 W(x) = 0, \quad (37)$$

with BCs

$$\begin{aligned} W(0) &= 0 \\ W'(0) &= 0 \\ W''(1) &= 0 \\ W'''(1) &= -m\omega^2 W(1) + kW(1), \end{aligned} \quad (38)$$

the solutions to which yield the natural frequencies ω_i and normal modes W_i ($i = 1, 2, 3, \dots$). Substituting the i^{th} natural frequency and normal mode in Eq. (37), multiplying by the j^{th} normal mode, and integrating over the spatial domain of the problem (the length of the beam), we get

$$\int_0^1 W_j W_i'''' dx - \omega_i^2 \int_0^1 W_j W_i dx = 0. \quad (39)$$

Integrating by parts two times and using the BCs (Eq. 38), we obtain

$$\int_0^1 W_i'' W_j'' dx + kW_i(1)W_j(1) = \omega_i^2 \left[\int_0^1 W_i W_j dx + mW_i(1)W_j(1) \right]. \quad (40)$$

Given that in this case $\omega_i \neq \omega_j$ for $i \neq j$, swapping the indices i and j and subtracting the result from the above yields the orthogonality condition satisfied by the normal modes:

$$\int_0^1 W_i W_j dx + mW_i(1)W_j(1) = \delta_{ij}. \quad (41)$$

Substitution of the above into Eq. (40) then yields the additional condition:

$$\int_0^1 W_i'' W_j'' dx + kW_i(1)W_j(1) = \omega_i^2 \delta_{ij}. \quad (42)$$

It can be immediately observed that, subject to the appropriate assumptions on the stiffness k , Eqs. (41) and (42) have the same form as Eqs. (9).